

Revision 1 (#5603) - Submitted to American Mineralogist

## Constraints on the solid solubility of Hg, Tl and Cd in arsenian pyrite

Artur P. Deditius<sup>1,\*</sup> and Martin Reich<sup>2,3</sup>

<sup>1</sup>*Murdoch University, School of Engineering and Information Technology, 90 South Street,*

*Murdoch, Western Australia 6150, Australia*

<sup>2</sup>*Department of Geology, FCFM, Universidad de Chile, Santiago, Chile*

<sup>3</sup>*Andean Geothermal Center of Excellence, FCFM, Universidad de Chile, Santiago, Chile*

\*Corresponding author: E-mail: [A.Deditius@murdoch.edu.au](mailto:A.Deditius@murdoch.edu.au); Tel.: +61 8 9360 2525.

### Abstract

Arsenic-rich (arsenian) pyrite can contain up to tens of thousands of parts per million (ppm) of toxic heavy metals such as Hg, Tl and Cd, although few data are available on their solid solubility behaviour. When a compilation of Hg, Tl and Cd analyses from different environments are plotted along with As in a  $M(\text{Hg, Tl, and Cd})\text{-As}$  log-log space, the resulting wedge-shaped distribution of datapoints suggests that the solid solubility of the aforementioned metals is strongly dependent on the As concentration of pyrite. The solid solubility limits of Hg in arsenian pyrite – i.e., the upper limit of the wedge-shaped zone in compositional space – are similar to the one previously defined for Au by Reich et al. (2005) ( $C_{\text{Hg,Au}} = 0.02C_{\text{As}} + 4 \times 10^{-5}$ ), whereas the solubility limit of Tl in arsenian pyrite is approximated by a ratio of  $\text{Tl/As} = 1$ . In contrast, and despite a wedge-shaped distribution of Cd-As datapoints for pyrite in Cd-As log-log space, the majority of Cd analyses reflect the presence of mineral particles of Cd-rich sphalerite and/or CdS. Based on these data, we show that arsenian pyrite with  $M/\text{As}$  ratios above the solubility limit of Hg and Tl contain nanoparticles of HgS, and multimetallic Tl-Hg mineral nanoparticles. These results indicate that the

27 uptake of Hg and Tl in pyrite is strongly dependent on As contents, as it has been previously  
28 documented for metals such as Au and Cu. Cadmium, on the other hand, follows a different  
29 behaviour and its incorporation into the pyrite structure is most likely limited by the precipitation of  
30 Cd-rich nanoparticulate sphalerite. The distribution of metal concentrations below the solubility  
31 limit suggests that hydrothermal fluids from which pyrite precipitate are dominantly undersaturated  
32 with respect to species of Hg and Tl, favouring the incorporation of these metals into the pyrite  
33 structure as solid solution. In contrast, the formation of metallic aggregates of Hg and Tl or mineral  
34 nanoparticles in the pyrite matrix occur when Hg and Tl locally oversaturate with respect to their  
35 solid phases at constant temperature. This process can be kinetically enhanced by high-to-medium  
36 temperature metamorphism and thermal processing or combustion, which demonstrates a retrograde  
37 solubility for these metals in pyrite.

38

39 **Keywords:** mercury, thallium, cadmium, arsenic, pyrite, nanoparticles

40

41

## Introduction

42 Pyrite ( $\text{FeS}_2$ ) is the most common sulphide in the upper crust and can host from a few parts  
43 per million (ppm) up to weight percent (wt. %) levels of heavy metals and metalloids such as As,  
44 Hg, Tl and Cd (Rickard and Luther 2007; Deditius et al. 2008; Leticariu et al. 2011, Keith et al.  
45 2016). Mineral processing of gold-bearing arsenian pyrite and combustion of pyrite-bearing coal  
46 result in the liberation of these toxic elements into the environment posing significant threats to the  
47 biosphere (Ikramuddin et al. 1986; Wang et al. 2010; Kolker 2012). For example, 810 Mt/year of  
48 Hg are released into the atmosphere as a result of coal combustion (Pirrone et al. 2010), and  
49 industrial processing is responsible for the mobilization of 2000-5000 t/year of Tl (Kazantzis 2000;  
50 John Peter and Viraraghavan 2005). Furthermore, recent studies have estimated the emission of 4.7  
51 t/year of Cd from sulphide ore mining and 10 t/year in air from basic non-ferrous metals  
52 manufacture in Australia (Kyle et al. 2011). In the particular case of As, there are numerous studies

53 reporting natural and anthropogenic contamination of water and soil, and its effects on human  
54 health (Plant et al. 2014). Among the numerous toxicological effects of As and heavy metals (Tl, Hg  
55 and Cd) on biota, carcinogenic and brain dysfunction effects are considered some of the most  
56 important for human life (Kyle et al. 2011 and references therein).

57 In arsenian (As-rich) pyrite, previous studies have revealed that Hg and Tl tend to  
58 accumulate in zones where precious metals such as Au are concentrated, particularly, in low-  
59 temperature (<200 °C) sedimentary environments, and Carlin-type and epithermal Au deposits  
60 (Cline 2001; Emsbo et al. 2003; Reich et al. 2005; Barker et al. 2009; Deditius et al. 2011; Large et  
61 al. 2014). In contrast, it is known that Cd partitions into sphalerite (ZnS) and/or Cd-sulphides under  
62 higher-temperature magmatic-hydrothermal conditions and submarine hydrothermal vents (Cook et  
63 al. 2009; Pass 2010; Lockington et al. 2014; Revan et al. 2014; Keith et al. 2016). Metal  
64 incorporation into pyrite is complex and studies have shown that both speciation (structurally-bound  
65 vs. nanoparticulate) and concentration (ppm to weight % levels) are controlled by the incorporation  
66 of As into the structure (Reich et al. 2005; Deditius et al. 2014). For example, transmission electron  
67 microscopy (TEM) observations have revealed that metals like Au (and associated Hg) in pyrite are  
68 commonly hosted as nanoparticles (NPs) or are incorporated into solid solution, particularly in the  
69 As-rich growth bands and sectors (Palenik et al. 2004; Deditius et al. 2011). The coupled  
70 geochemical behaviour between metals and arsenic (e.g., Au vs. As) is clearly exemplified by the  
71 solid solubility model proposed by Reich et al. (2005) for Carlin-type and epithermal Au deposits  
72 where the Au content of pyrite is a function of As content. Using micro-analytical (EMPA, SIMS)  
73 and spectroscopic analyses (synchrotron XANES), the aforementioned authors showed that when  
74 Au-As datapoints are plotted on an Au vs. As log-log space, an As-dependent Au solubility curve  
75 defines two fields where Au is present as native Au nanoparticles (above the solubility curve) or as  
76 solid solution Au<sup>+1</sup> (below the solubility curve). Recently, this solubility limit was extended to all  
77 types of ore deposits containing pyrite (Deditius et al. 2014), and recent studies have reported a  
78 significant relation between As and metals such as Ag and Cu, to name a few (Reich et al. 2010,

79 2013).

80 Despite these advances, to the best to our knowledge there is no detailed information on the  
81 behaviour of Hg, Tl and Cd in pyrite, and their potential dependence on the contained As of the  
82 pyrite mineral host. In one of the very few studies documenting this particular association, [Zhou et  
83 al. \(2005\)](#) report elevated concentrations of Tl (up to 3.5 wt. %) in pyrite from the Xiangquan  
84 deposit in China that correlate with high concentrations of As (up to 2.6 wt. %) and Hg (up to 400  
85 ppm). In this Tl deposit, thallium occurs mainly in As and Hg-rich pyrite with minor amounts of  
86 lorandite (TlAsS<sub>2</sub>) and hutchinsonite (TlFeS<sub>2</sub>), strongly suggesting a complex incorporation of these  
87 metals in pyrite. Furthermore, experimental evidence suggests that sorption of Cd and other soft  
88 Lewis acids in the natural environment suppresses FeS<sub>2</sub> oxidation, and may retard the release of  
89 acidity and trace metals to the environment ([Bostick et al. 2000](#)). However, the particular role of As  
90 during Hg, Tl and Cd uptake and release remains obscure. This significant gap in understanding of  
91 the geochemical behaviour of Hg, Tl and Cd in arsenian pyrite encouraged us to test the hypothesis  
92 that these metals have solid solubility behaviour in arsenian pyrite that is similar to that of Au.

93

#### 94 **Coupled geochemistry of Hg, Tl, Cd and As in pyrite**

95 A compilation of previously published electron microprobe analyzer (EMPA), secondary ion  
96 mass spectrometry (SIMS) and laser ablation inductively coupled plasma mass spectrometry (LA-  
97 ICP-MS), proton-induced X-ray emission (PIXE), instrumental neutron activation analysis (INAA)  
98 data was used to constrain elemental relations between Hg, Tl, Cd and As in pyrite ([Table 1](#)). Data  
99 was compiled for pyrite from a variety of environments including porphyry Cu, epithermal and  
100 orogenic Au, volcanogenic massive sulphide (VMS), Witwatersrand and Carlin-type Au deposits,  
101 and pyrite-bearing metamorphic rocks, sedimentary sequences and coal beds. This work provides a  
102 compilation of pyrite analyses obtained by methods that combine low detection limits (ppm levels)  
103 such as SIMS, LA-ICP-MS and PIXE, with high spatial resolution techniques (EMPA).

104 Concentrations of Hg, Tl, and Cd in pyrite in these environments vary from below the

105 detection to ~15,000 ppm. With the exception of pyrite from the Mt. Polley porphyry Cu-Ag-Au  
106 deposit, more than 99% of the metals' analyses in arsenian pyrite plot below the  $M/As = 1$ ; where  $M$   
107 = Hg, Tl and Cd (Fig. 1A-C). In all three cases, the distribution of the data points approximates the  
108 wedge-shaped zone interpreted as the solid solubility limit for Au in arsenian pyrite (Reich et al.  
109 2005; Deditius et al. 2014). The highest content of Hg and Tl was measured in pyrite from Carlin-  
110 type, epithermal and coal deposits, while the highest concentrations of Cd (up to ~1000 ppm) occur  
111 in pyrite from porphyry Cu deposits, VMS deposits, and sedimentary environments (Figs. 1A-B).  
112 No data for Cd is available for pyrite from Carlin-type deposits.

113 Mercury. Figure 1A displays a positive trend of increasing Hg and As contents in pyrite. The  
114 lowest content of Hg, ~0.01-10 ppm, was reported for pyrite from porphyry (Cu-Au-Mo) deposits,  
115 sedimentary pyrite, and orogenic Au deposits (Pass 2010; Franchini et al. 2015; Marin-Carbonne et  
116 al. 2014; Paleonova et al. 2015). In contrast, the highest amounts of Hg were found in pyrite from  
117 Carlin-type and epithermal Au deposits (Cline 2001; Emsbo et al. 2003; Deditius et al. 2011).  
118 Except for a few outliers, almost all the data plot below the  $Hg/As = 1$  limit (Fig. 1A). As a  
119 reference, the As-dependent solubility limit of Au is shown. EMPA data of Hg-rich (500-1,900 ppm)  
120 arsenian pyrite from the Lone Tree Au deposit in Nevada plot above the solubility limit defined by  
121 Reich et al. (2005) (“nanoparticle field”, NP), and close to the ratio  $Hg/As = 1$  that marks the upper  
122 limit of the datapoint cloud (Fig. 1A, black triangles, circled and labelled “NP”). High-resolution  
123 TEM observations of the high-Hg pyrite revealed the presence of HgS nanoparticles (NPs)  
124 (Deditius et al. 2011). Therefore, analytical data are indicative of the occurrence of Hg-bearing NPs  
125 when Hg and As concentrations exceed the solubility limit in pyrite by Reich et al. (2005), or  $Hg/As$   
126 ratios approach unity (Fig. 1A). A similar behaviour was observed for Hg-bearing metamorphic  
127 pyrite, where Hg partitions into the low-temperature melt (< 420°C, greenschist facies) and  
128 recrystallizes as complex Tl-Hg-As-Sb-(Ag,Cu)-Pb sulfosalts in pyrite samples from Alpi Apuane  
129 (Biagioni et al. 2013). These analyses also plot above the solubility limit (in the NPs field), close to  
130  $Hg/As = 1$  (Fig. 1A, open squares, circled and labelled “NP”).

131 In contrast, high Hg and As contents of pyrite in the Deep Star Carlin-type deposit in  
132 Nevada plot below the solubility defined by Reich et al. (2005), and at Hg/As ratios lower than 1  
133 (Hg: 900-14,300 ppm, As: >50,000 ppm As, Fig. 1A). TEM observations and XANES analyses of  
134 these anomalously Hg-As-rich pyrite samples show no evidence of Hg-bearing NPs (Reich et al.  
135 2005). Therefore, Hg-As datapoints plotting below the solubility limit are interpreted to contain  
136 structurally bound or solid solution Hg (Fig. 1A, oval, labelled “SS”).

137 Our analysis shows, as a first approximation, that the As-dependent solubility limit of Au in  
138 Figure 1A is a good proxy to evaluate the speciation of Hg in pyrite, i.e., Hg is incorporated in solid  
139 solution at lower Hg/As ratios, while its incorporation is favoured as NPs at high Hg/As ratios. A  
140 similar behaviour/feature of solid solubility for Hg and Au in pyrite is expected, considering the  
141 ability of these two metals to form alloys and amalgams even at the nanoscale (Schopf et al. 2015).  
142 However, it is important to mention that this behaviour is observed in the higher range of  
143 concentrations of As and Hg, i.e., > 1000 ppm and >100 ppm, respectively (Fig. 1A). Unfortunately,  
144 no nano-analytical and spectroscopic information of Hg and As in pyrite is available for samples  
145 characterized by lower amounts of these elements (i.e., <100 ppm for both Hg and As).

146 Thallium. Figure 1B shows that Tl-As data of pyrite from different environments form a  
147 similar wedge-shaped zone, limited above by a line of approximate slope Tl/As=1. Pyrite from  
148 Carlin-type and coal deposits contain the highest amount of Tl, while the concentrations of Tl in  
149 pyrite from porphyry Cu and orogenic Au deposits are generally below 1 ppm. This can be  
150 attributed to the volatile nature of Tl and its strong affinity towards organic matter. A recent review  
151 of the composition of sedimentary pyrite by Large et al. (2014) revealed a broad range of Tl  
152 concentrations varying from 0.1 ppm – 10,000 ppm. The majority of these analyses plot below a  
153 Tl/As ratio of 1 (Fig. 1B). Similarly to Hg, Tl-bearing NPs in pyrite were observed in metamorphic  
154 settings, suggesting that metamorphism induced the mobilization of multimetallic melts (Bagnioni  
155 et al. 2013). These representative Tl-As analyses plot homogeneously above the indicated Tl/As = 1,  
156 over range of As concentrations from 10’s to 10,000’s ppm. Unfortunately, there is no

157 nanostructural or spectroscopic data that would help constrain the speciation and/or its structural  
158 position of Tl in arsenian pyrite. However, [Kouzmanov et al. \(2010\)](#) did not notice any Tl particles  
159 (or other metallic nanonuggets) during LA-ICP-MS profiling of pyrite from the Rosia Poeni  
160 porphyry Cu deposit. Therefore, acknowledging the fact that it is not straightforward to establish  
161 precise Tl-As solubility relations with the available data, we suggest that the upper limit ratio Tl/As  
162 = 1 may represent, as a first approximation, the solid solubility limit of Tl in arsenian pyrite (i.e.,  
163 analyses plotting below Tl/As ratios of 1 represent Tl in solid solution, while datapoints plotting  
164 above this limit are most likely related to the presence of Tl-bearing nano-inclusions).

165 Cadmium. Similarly to Hg and Tl, the majority of Cd data points cluster in a wedge-shaped  
166 zone and plot below the  $M/As$  ratio of 1 ([Fig. 1C](#)). The amount of Cd in pyrite varies significantly  
167 between the different types of ore deposits. The highest contents of Cd, > 5 ppm, have been  
168 reported for pyrite from porphyry Cu deposits, hydrothermal vents in mid-ocean ridges, and  
169 volcanic precipitates ([Yudovskaya et al. 2006](#); [Pass 2010](#); [Revan et al. 2014](#); [Keith et al. 2016](#)),  
170 while the lowest amounts (below ppm-levels) have been found in As-poor pyrite from epithermal  
171 Au deposits ([Franchini et al. 2015](#)) ([Fig. 1B](#)). Most of the datapoints come from sedimentary  
172 settings, where variable Cd concentrations spread from ppb- up to thousands of ppm-levels ([Large  
173 et al. 2014](#)) ([Fig. 1C](#)). Unfortunately, there is no data available to constraint the structural behaviour  
174 of Cd in arsenian pyrite or predict the presence of Cd NPs vs. solid solution incorporation.  
175 However, it has been suggested that Cd partitions into sulphide nano- and/or micro-particles and  
176 crystallizes as CdS and/or Cd-rich sphalerite in pyrite under wide range of temperatures (from 250-  
177 650 °C) conditions ([Hannington et al. 1988, 1991](#); [Genna and Gaboury 2015](#); [Keith et al. 2016](#)).

178 Therefore, it is likely that higher concentrations of Cd contents in pyrite from porphyry Cu  
179 deposits, hydrothermal vents (VMS) and volcanic precipitates ([Fig. 1C](#)) represent inclusions of Cd-  
180 sulfides and or sphalerite, as previously reported ([Hannington et al. 1988, 1991](#); [Genna and  
181 Gaboury 2015](#); [Keith et al. 2016](#)). The datapoints representing Cd in sphalerite NPs plot in the field  
182 of nanoparticles and solid solution, Thus, it is likely the wedge-shaped distribution of the Cd data



183 points in the Cd-As log-log space below the Cd/As = 1 ratio does not indicate a solubility limit,  
184 despite its position to be similar to the one for Au, Hg, and Tl (Fig. 1C).

185

### 186 **Intrinsic controls on the solubility limit of Hg, Tl, and Cd in arsenian pyrite**

187 Our compilation and review of the available data on the behaviour of Hg, Tl and Cd in  
188 arsenian pyrite has revealed the presence of similar compositional features previously reported for  
189 Au (e.g., Reich et al. 2005; Deditius et al. 2014). Perhaps the most noticeable first-order feature  
190 observed is the wedge-shaped pattern that arises when Hg, Cd and Tl concentrations are plotted  
191 against As. These wedge-shaped zones are limited above by a solubility limit in compositional log-  
192 log space, which can be approximated either by the solubility relation found for Au by Reich et al.  
193 (2005) (for Hg, Cd and Au:  $C_{\text{Hg,Cd,Au}} = 0.02C_{\text{As}} + 4 \times 10^{-5}$ , see curve in Figure 1) or, for the particular  
194 case of Tl, by a Tl/As ratio of  $\sim 1$  (Fig. 1B). While these relationships suggest some common and  
195 fundamental mechanisms controlling the uptake as Au, Hg, and Tl into arsenian pyrite, the  
196 behaviour of Cd seem to be controlled by the precipitation of mineral nanoparticles of sphalerite  
197 and/or Cd-sulphides and is more likely related to fluid-mineral interaction. The described features  
198 are relevant to explore the mechanisms of incorporation of Hg, Tl and Cd into pyrite, but may also  
199 have a similar impact when evaluating the release of such metals from the arsenian pyrite matrix.

200 It has been documented that the incorporation of anionic ( $\text{As}^{1-}$ , Simon et al. 1999; Abraitis et  
201 al. 2004) or cationic ( $\text{As}^{3+}$ , Deditius et al. 2008) arsenic species into the pyrite structure facilitates  
202 substitution of other metals, most noticeable Au. Similar behaviour reported here for the heavy  
203 metals Hg and Tl in arsenian pyrite may be related to the relatively small differences in their crystal  
204 radii with respect to Au. Substitutional mechanisms discussions are commonly limited to the formal  
205 charges, which should be treated with caution considering the covalent type of bonding in  
206 sulphides, i.e.,  $\text{Au}^+$  and  $\text{Au}^{3+}$  (0.157 and 0.099 nm, respectively),  $\text{Hg}^+$  and  $\text{Hg}^{2+}$  (0.133 and 0.116  
207 nm, respectively),  $\text{Tl}^+$  and  $\text{Tl}^{3+}$  (0.164 and 0.1025 nm, respectively), (data after Shannon 1976, for  
208 octahedral coordination).



209           The incorporation of Hg and Tl depends on the presence of other substitutions in the pyrite  
210 structure. Therefore, changes in the semi-conducting behaviour of pyrite surfaces during crystal  
211 growth may have a significant impact on metal uptake, i.e., As and Sb promote *p*-type conductivity,  
212 while the presence of divalent metals such as Co and/or Ni in the structure induces *n*-type  
213 conductivity (Pearce et al. 2006 and references therein). Substitution of As for S in the tetrahedral  
214 position generates a hole in the Fe *d*-like valence band, which makes As an acceptor capable of  
215 accommodating one electron from the valence band, and as a consequence, a charge carrier. Such  
216 contrasting As vs. Co/Ni-rich areas may occur within a single crystal of pyrite. In addition, the  
217 increase in As contents in pyrite expands the unit cell and creates structural distortion. Therefore, a  
218 combination of the electrical and crystal-chemical properties of As may generate favourable  
219 conditions promoting the incorporation of heavy metals in pyrite in natural environments (Lehner et  
220 al. 2006, 2012). In the case of synthetic materials, it has been reported that *p*-type conductivity  
221 promotes high solid solubility of Au in semiconductors matrices such as silicon (O'Shaughnessy et  
222 al. 1974). Because *p*-type conductivity occurs in phosphorous-doped synthetic pyrite (Blenk et al.  
223 1993), it is very likely that the effects on metal behaviour are similar. In particular, phosphorous-  
224 bearing pyrite crystals have complex morphologies such as combinations of {111}, {110} and  
225 {100} forms that have also been observed in natural As and Au-rich hydrothermal pyrites  
226 (Chouinard et al. 2005). However, the influence of As on pyrite morphology remains ambiguous, as  
227 some authors report enhanced development of the {111} face (Sunagawa and Takahashi 1955),  
228 while others document higher contents of As in |hk0| sectors (Chouinard et al. 2005).

229           The other important factor that may regulate the amount of impurities in the pyrite structure  
230 is the size of the single crystals, which can be as small as 8 nm (Deditius et al. 2008). Material  
231 science provides evidence for nanoparticulate semiconductors that experience self-purification  
232 resulting in the expulsion of the non-stoichiometric impurities/dopants towards the grain boundaries  
233 (Erwin et al. 2005 and references therein). This feature is consistent with the occurrence of  
234 “invisible” (i.e., refractory) Tl in hydrothermal coarse-grained pyrite from Xiangquan thallium

235 deposit (China), which contains up to 35,000 ppm. In contrast, the amounts of Tl, Hg and Cd in the  
236 colloidal form of pyrite in this deposit were below 9,300 ppm; 400 and 230 ppm, respectively  
237 (Zhou et al. 2005). Such behaviour is mainly controlled by the surface morphology, shape of the  
238 nanocrystals, and surfactants in the solution. While in synthetic systems the diffusion of the trace  
239 element (Mn) in semiconductors (CdSe) around temperature of 300 °C is negligible, 1-3 Å in short  
240 time (1h) (Jamil and Shaw 1994), the equilibration and homogeneous distribution of the trace  
241 element within individual nanoparticles can be achieved over the geological time scale (Reich et al.,  
242 2006; Deditius et al. 2008; González-Jiménez et al., 2015). Moreover, it was found that the  
243 formation of trace element-rich semiconducting NPs - with homogeneously distributed doping  
244 element - is possible when the trace element is adsorbed on the growing surface of the nanocrystal  
245 (Erwin et al. 2005). Consequently, the rate of kinetically controlled growth of pyrite must exceed  
246 the rate of equilibration and removal of the impurities to accommodate Au, Hg and Tl in the crystal  
247 structure. This kinetically controlled formation of pyrite under lower temperature conditions (e.g.,  
248 collomorphic pyrite, Huston et al. 1995; Abraitis et al. 2004), promotes distortion of the pyrite  
249 structure and incorporation of higher quantities of large metals. This is envisaged by a positive  
250 correlation between Tl (up to about 8,000 ppm) and As in porous pyrite associated with the (As,Sb)-  
251 growth zones, which have been interpreted to be a result of precipitation from hydrothermal fluids  
252 originating from multiple sources (Ingham et al. 2014). It is likely that the presence of As-  
253 promoting distortion and surface modification enables incorporation of the large cations, Au, Hg,  
254 and Tl, via stoichiometric or nonstoichiometric substitutions involving the formation of vacancies  
255 (Chouinard et al. 2005; Deditius et al. 2008), or nanoscale phase decomposition such as  
256 polycrystalline pyrite nano-aggregates (Palenik et al. 2004).

257

### 258 **Role of fluid composition and temperature**

259 Firstly, the chemical composition of the fluid is one of the main factors that control metal  
260 uptake during pyrite growth. For example, the presence of Hg-rich growth zoning on pyrite in

261 Carlin-type and epithermal Au deposits is indicative that the deposition of Hg is restricted by its  
262 availability in the fluid, similar to Au (Barker et al. 2009). In sedimentary environments, pyrite is a  
263 natural sink for Hg during coal formation, where recrystallized pyrite can incorporate up to 7600  
264 ppb of Hg (Hamington et al. 1991; Lefticariu et al. 2011). In both examples, the mechanism of Hg  
265 incorporation would involve the breakdown of aqueous Hg complexes and the adsorption of Hg  
266 species onto the growing pyrite surfaces. It is likely that this process is enhanced by local fluid  
267 oxidation (Chouinard et al. 2005; Barker et al. 2009) and the presence of As in the mineralizing  
268 fluid (see previous section).

269 Chemisorption of metal species onto pyrite surfaces can result in a highly efficient  
270 mechanism for sequestering metals from mineralizing fluids. Erhardt et al. (2000) reported partial  
271 oxidation of pyrite surfaces during adsorption of  $\text{Hg}^{2+}$  with the formation of inner surface  
272 complexes. This mechanism is supported by XPS and XAS studies of Hg incorporation into pyrite,  
273 which revealed formation of surface complexes between S(-I) and Hg(II) (Behra et al. 2001), and  
274 Hg-Cl complexes on the pyrite surface (Bower et al. 2008). No native Hg or Hg-sulphides were  
275 found in these studies. Unlike Hg (or Tl), the relatively small amounts of Cd present in pyrite may  
276 be a result of the decreasing efficiency of Cd uptake with increasing concentration in the pyrite  
277 surface (Parkman et al. 1999). The lack of separation between the datapoints representing  
278 nanoparticulate Cd-rich sphalerite and Cd in solid solution in pyrite (Fig. 1C) suggests that Cd  
279 incorporation into pyrite is not controlled by solid state solubility rules. In contrast, it is suggested  
280 that sphalerite NPs form at the pyrite-fluid interface due to rapid precipitation from the Cl-depleted  
281 fluids, which become supersaturated with respect to (Zn,Cd)-sulphides (Reich et al. 2013; Keith et  
282 al. 2016). In addition, Bostick et al. (2000) proposed reconstruction and disproportionation of pyrite  
283 surface that resulted in the mixture of native sulphur, Fe-hydroxides and CdS, supporting  
284 preferential formation of particulate sulphides rather than incorporation into the structure as solid  
285 solution (Fig. 1C).

286 Secondly, the temperature of pyrite formation or subsequent metamorphism is a key factor

287 controlling the metal budget of pyrite in geologic environments. The identification of particulate Hg  
288 and Tl in pyrite in low-temperature metamorphic rocks [Bagioni et al. \(2013\)](#) demonstrates that low-  
289 temperature recrystallization processes involving trace element-rich pyrite are one of the most  
290 important factors controlling the post-entrapment mobilization of these metals ([Fig. 1](#)). The  
291 temperature of mobilization depends on the association of metals; i.e., the larger the numbers of  
292 metals, characterized by low-temperature melting, chemically connected in the structure of the  
293 hosting sulphide the lower the melting temperature of the sulphide domain ([Tomkins et al. 2007](#));  
294 the melting temperatures of Tl-Au, Hg-Au, and Bi-Au systems are as low as 147 °C, 39 °C, and 241  
295 °C respectively ([Okamoto and Massalski 1987](#)).

296         The in-situ thermal stability experiments by [Reich et al. \(2006\)](#) are one of the very few  
297 studies that document the effect of temperature on metal nanoparticle stability in pyrite. In this  
298 study, native Au NPs of ~10 nm begin to dissolve in the As-rich pyrite matrix and diffusively  
299 growth at the expense of smaller ones at temperatures close to 400 °C. Therefore, it is likely that  
300 Hg, Tl, and Cd may be liberated much easier from the structure of a distorted, nanoparticulate, As-  
301 rich pyrite matrix. However, it is expected that these metals will behave differently within  
302 multimetallic NPs with the increase of temperature as envisaged by separation of Pt and Au,  
303 diffusion of Au through the Ag<sub>2</sub>S, and its Ostwald ripening-based recrystallization on the surface of  
304 Ag<sub>2</sub>S ([Yang and Ying 2010](#)). Alternatively, the aggregates of separate mineral NPs will form alloys  
305 with the temperature increase ([Bonifacio et al. 2015](#)). For example, given the paucity of information  
306 on the occurrence of Tl NPs in well-investigated pyrite samples suggests that Tl preferentially  
307 dissolves into the pyrite matrix ([see Fig 1B](#)), rather than forming separate domains of Tl-sulfides.  
308 This might be related to the possible higher oxidation state of Tl<sup>3+</sup> in collomorphic pyrite ([Huston et  
309 al. 1995](#)). In addition, the decrease in the Fe content in pyrite will promote formation of “liquid-  
310 like” As-Fe-S NPs entrapped in the arsenian pyrite structure ([Deditius et al. 2009](#)), which in turn  
311 may sequester migrating/diffusing metals. The separation of metallic nanodomains is also supported  
312 by positive correlation between Cd and Zn in pyrite from paleo-chimneys, which suggests that Cd is

313 incorporated by micro-inclusions of sphalerite (Revan et al. 2014; Genna and Gaboury 2015; Keith  
314 et al. 2016). In addition, under hydrothermal conditions >344 °C HgS (metacinnabar) precipitates  
315 from Hg<sup>2+</sup>-aqueous solutions rich in S(-II), while cinnabar is forming below the indicated  
316 temperature (Barnes and Seward 1997).

317 Consequently, the behaviour of Hg, Tl and Cd in arsenian pyrite is an outcome of primary  
318 intrinsic factors, in the studied case, the presence of As-rich pyrite surface and extrinsic features of  
319 the environment in which pyrite forms. These include: (i) “fluid”-control, i.e., chemical  
320 composition of the hydrothermal fluid; which also impacts the surface morphology and thus  
321 controls chemisorption and processes of “solid solution” incorporation, and (ii) a temperature  
322 control that influences stability of the matrix, formation and stability of NPs.

323

324

### Geochemical implications and future studies

325 Based on the aforementioned discussion, we propose a conceptual model that describes the  
326 behaviour of Hg, Tl and Au in the metal-As-T space (Fig. 2). Figure 2 shows that the two fields NPs  
327 and solid solution are separated by bowl-like solubility surface with the crest of solubility limit after  
328 Reich et al. (2005) projected from the As-Au space. Note that this solubility limit crest may shift  
329 up- and downwards along the solubility plane with the changes in the temperature (Fig. 2). The  
330 increase in temperature is likely to cause metal mobilization from pyrite during recrystallization and  
331 high-temperature alteration under metamorphic conditions reported for orogenic Au deposits (Sung  
332 et al. 2009). On the contrary, cooling will promote formation of metallic mineral NPs in case of As-  
333 poor pyrite across all geological environments as discussed in detail by Deditius et al. (2014).

334 The recognition of solid solubility limits for Hg, and Tl, and the presence of micro-to-  
335 nanoparticulate Cd in pyrite provide new insights into the environmental sequestration of Hg, Tl  
336 and Cd. Until now, the geochemical behaviour of Hg and Tl in pyrite was exclusively linked with  
337 the presence mineral particles and/or (non) stoichiometric structural substitutions. We suggest that  
338 the uptake of Hg, and Tl into arsenian pyrite is strongly tied to presence of As, and that the

339 occurrence of these metals as nanoparticles vs. solid solution in pyrite may be predicted if the solid  
340 solubility limits are precisely determined using a combination of experimental, analytical and  
341 spectroscopic data. The distribution of most of the analyses below the solubility limit suggests that  
342 Hg and Tl are preferentially incorporated as structurally-bound species in pyrite, probably through  
343 chemisorption processes in aqueous solutions that are mostly undersaturated with respect to their  
344 native metals species or mineral NPs (Figs. 1 and 2). Furthermore, the restricted occurrence of Hg,  
345 and Tl nanoparticles in arsenian pyrite, as predicted by the solid solubility limits, is most likely the  
346 result of local over-saturation of aqueous solutions and/or post-entrapment modifications resulting  
347 from changes in temperature during diagenesis or metamorphism. The documented lack of a  
348 solubility limit for Cd in arsenian pyrite can be extended to other elements, e.g., Pb, Ag, Te and Sb,  
349 which have been detected in significant concentrations in pyrite but predominantly occur as micro-  
350 to-nanoscale inclusions in porous zones (Pačevski et al. 2012).

351         Considering the scarce nanostructural and largely non-systematic information available for  
352 hazardous metals in pyrite, future studies aiming to elucidate the geochemical cycle of these  
353 elements should incorporate a combination of experimental approach and studies of representative  
354 natural samples involving: i) determination of the major and trace element composition using a  
355 combination of EMPA, SIMS and/or LA-ICP-MS, ii) preliminary tests to target NPs (e.g., FE-SEM  
356 observations, and depth profiling using SIMS or LA-ICP-MS), iii) sampling prospective areas of  
357 pyrite using focused-ion beam (FIB), iv) TEM studies to detect, image and resolve the crystal-  
358 chemistry of NPs, vi) synchrotron-based XANES and EXAFS studies to determine the oxidation  
359 state and/or speciation of trace elements.

360

### 361 **Acknowledgments**

362 Authors are indebted to Ian Swainson, Nigel Cook and Ross Large for insightful comments that  
363 greatly improved the quality of the manuscript. Martin Reich acknowledges support from MSI grant  
364 “Millennium Nucleus for Metal Tracing Along Subduction (NC130065)”, FONDAP project

365 15090013 “Centro de Excelencia en Geotermia de los Andes, CEGA”, and FONDECYT grant  
366 1130030.

367

368 **References**

369 Abraitis, P.K., Patrick, R.A.D., and Vaughan, D.J. (2004) Variations in compositional, textural and  
370 electrical properties of natural pyrite: a review. *International Journal of Mineral Processing*, 74,  
371 41-59.

372 Agangi, A., Hofman, A., and Wohlgemuth-Ueberwasser, C.C. (2013) Pyrite zoning as a record of  
373 mineralization in the Ventersdorp contact reef, Witwatersrand Basin, South Africa. *Economic*  
374 *Geology*, 108, 1243-1272.

375 Bagioni, C., D’Orazio, M., Vezzoni, S., Dini, A., and Orlandi, P. (2013) Mobilization of Tl-Hg-As-  
376 Sb-(Ag,Cu)-Pb sulfosalt melts during low-grade metamorphism in the Alpi Apuane (Toscany,  
377 Italy). *Geology*, 41, 747-750.

378 Barker, S.L.L., Hickey, K.A., Cline, J.S., Dipple, G.M., Kilburn, M.R., Vaughan, J.R., and Longo,  
379 A.A. (2009) Uncloaking invisible gold: Use of nano-SIMS to evaluate gold, trace elements, and  
380 sulphur isotopes in pyrite from Carlin-type gold deposits. *Economic Geology*, 104, 897-904.

381 Barnes, H.L., and Seward, T.M. (1997) Geothermal systems and mercury deposits. In:  
382 *Geochemistry of Hydrothermal Ore Deposits*, 3<sup>rd</sup> ed. Barnes HI (ed) Wiley, p 699-736.

383 Behra, P., Bonnissel-Gissingner, P., Alnot, M., Revel, R., and Erhardt, J.J. (2001) XPS and XAS  
384 study of the sorption of Hg(II) onto pyrite. *Langmuir*, 17, 3970-3979.

385 Berner, Z.A., Puchelt, H., Nöltner, T., and Kramaer, U. (2013) Pyrite geochemistry in the Taoracian  
386 Posidonia Shale of south-west Germany: Evidence for contrasting trace-element patterns of  
387 diagenetic and syngenetic pyrites. *Sedimentology*, 60, 548-573.

388 Blenk, O., Bucher, E., and Willeke, G. (1993) p-type conduction in pyrite single crystals prepared  
389 by chemical vapour transport. *Applied Physics Letters*, 62, 2093.

390 Bonifacio, C.S., Carencio, S., Wu, C.-H., House, S.D., Bluhm, H., and Yang, J.C. (2015) Thermal



- 391 stability of core-shell nanoparticles: A combined in situ study by XPS and TEM. *Chemistry of*  
392 *Materials*, DOI: 10.1021/acs.chemmater.5b01862.
- 393 Bostick, B.C., Fendorf, S., and Fendorf, M. (2000) disulphide disproportionation and CdS  
394 formation upon cadmium sorption on FeS<sub>2</sub>. *Geochimica et Cosmochimica Acta*, 64, 247-255.
- 395 Bower, J., Savage, K.S., Weinman, B., Barnett, M.O., Hamilton, W.P., and Harper, W.F. (2008)  
396 Immobilization of mercury by pyrite (FeS<sub>2</sub>). *Environmental Pollution*, 156, 504-514.
- 397 Cabral, A.R., Koglin, N., Strauss, H., Brätz, H., and Kwitko-Ribero, R. (2013) Regional sulphate-  
398 hematite-sulfide zoning in the auriferous Mariana anticline, Quadrilátero Ferrífero of Minas  
399 Gerais, Brazil. *Mineralium Deposita*, 48, 805-816.
- 400 Cepedal, A., Fuertes-Fuente, M., Martín-Izard, A., González-Instal, S., Barrero, M. (2008) Gold-  
401 bearing As-rich pyrite and arsenopyrite from the El Valle gold deposit, Asturias, northwestern  
402 Spain. *The Canadian Mineralogist*, 46, 233-247.
- 403 Chouinard, A., Paquette, J., and Williams-Jones, A.E. (2005) Crystallographic controls on trace-  
404 element incorporation in auriferous pyrite from the Pascua epithermal high-sulfidation deposit,  
405 Chile-Argentina. *Canadian Mineralogist*, 43, 951-963.
- 406 Cline, J.S. (2001) Timing of gold and arsenic sulfide mineral deposition at the Getchell Carlin-type  
407 gold deposit, North-Central Nevada. *Economic Geology*, 96, 75-89.
- 408 Cook, N.J., Ciobanu, C.L., Pring, A., Skinner, W., Shimizu, M., Danyushevsky, L., Saini-Eidukat,  
409 B., and Melcher, F. (2009) Trace and minor elements in sphalerite: A LA-ICP-MS study.  
410 *Geochimica et Cosmochimica Acta*, 73, 4761-4791.
- 411 Deditius, A.P., Utsunomiya, S., Renock, D., Ewing, R.C., Ramana, C.V., Becker, U., and Kesler,  
412 S.E. (2008) A proposed new type of arsenian pyrite: Composition, nanostructure and geological  
413 significance. *Geochimica et Cosmochimica Acta*, 72, 2919-2933.
- 414 Deditius, A.P., Utsunomiya, S., Ewing, R.C., and Kesler, S.E. (2009) Nanoscale “liquid” inclusions  
415 of As-Fe-S in arsenian pyrite. *American Mineralogist*, 94, 391-394.
- 416 Deditius, A.P., Utsunomiya, S., Kesler, S.E., Reich, M., and Ewing, R.C. (2011) Trace elements

- 417 nanoparticles in pyrite. *Ore Geology Reviews*, 42, 32-46.
- 418 Deditius, A.P., Reich, M., Kesler, S.E., Utsunomiya, S., Chryssoulis, S.L., Walshe, J., and Ewing,  
419 R.C. (2014) The coupled geochemistry of Au and As in pyrite from hydrothermal ore deposits.  
420 *Geochimica et Cosmochimica Acta*, 140, 644-670.
- 421 Deol, S., Deb, M., Large, R.R., Gilbert, S. (2012) LA-ICPMS and EMPA studies of pyrite,  
422 arsenopyrite and loellingite from the Bhukia-Jagpura gold prospect, southern Rajasthan, India:  
423 Implications for ore genesis and gold remobilization. *Chemical Geology*, 326-327, 72-87.
- 424 Ding, Z., Zheng, B., Long, J., Belkin, H.E., Finkelman, R.B., Chen, C., Zhou, D., and Zhou, Y.  
425 (2001) Geological and geochemical characteristics of high arsenic coals from endemic arsenosis  
426 areas in southwestern Guizhou Province, China. *Applied Geochemistry*, 16, 1353-1360.
- 427 Duchesne, J.C., Rouhart, A., Schoumacher, C., and Dillen, H. (1983) Thallium, nickel, cobalt and  
428 other trace elements in iron sulphides from Belgian lead-zinc vein deposits. *Mineralium  
429 Deposita*, 18, 303-313.
- 430 Ehrhardt, J.J., Behra, P., Bonnisel-Gissinger, P., and Alnot, M. (2000) XPS study of the sorption of  
431 Hg(II) onto pyrite FeS<sub>2</sub>. *Surface and Interface Analysis*, 30, 269-272.
- 432 Emsbo, P., Hofstra, A.H., Lauha, E.A., Griffin, G.L., and Hutchinson, R.W. (2003) Origin of high-  
433 grade gold ore, source of ore fluid components, and genesis of the Mickle and neighbouring  
434 Carlin-type deposits, Northern Carlin Trend, Nevada. *Economic Geology*, 98, 1069-1105.
- 435 Erwin, S.C., Zu, L., Haftel, M.I., Efros, A.L., Kennedy, T.A., and Norris, D.J. (2005) Doping  
436 semiconductor nanocrystals. *Nature*, 436, 91-94.
- 437 Franchini, M., McFarlane, C., Maydagán, L., Reich, M., Lentz, D.R., Mainert, L., and Bouhier, V.  
438 (2015) Trace metals in pyrite and marcasite from the Agua Rica porphyry-high sulfidation  
439 epithermal deposit, Catamarca, Argentina: Textural features and metal zoning at the porphyry to  
440 epithermal transition. *Ore Geology Reviews*, 66, 366-387.
- 441 Genna, D., and Gaboury, D. (2015) Deciphering the hydrothermal evolution of a VMS system by  
442 LA-ICP-MS using trace elements in pyrite: An example from the Bracemac-McLeod deposits,

- 443 Abitibi, Canada, and implications for exploration. *Economic Geology*, 110, 2087-2108.
- 444 González-Jiménez, J., Reich, M., Camprubí, A., Gervilla, F., Griffin, W.L., Colás, V., O'Reilly, S.Y.,  
445 Proenza, J.A., Martini, M., Pearson, N.J., Centeno-García (2015). Thermal metamorphism of  
446 mantle chromites and the stability of noble-metal nanoparticles. *Contributions to Mineralogy and*  
447 *Petrology*, 170, 15.
- 448 Griffin, W.L., Ashley, P.M., Ryan, C.G., Sie, S.H., and Suter, G.F. (1991) Pyrite geochemistry in the  
449 North Arm epithermal Ag-Au deposit, Queensland, Australia: A proton-microprobe study.  
450 *Canadian Mineralogist*, 29, 185-198.
- 451 Hannington, M. D., Thompson, G., Rona, P. A., and Scott, S. D. (1988) Gold and native copper in  
452 supergene sulfides from the Mid-Atlantic Ridge. *Nature*, 333, 64–66.
- 453 Hannington, M., Herzig, P., Scott, S., Thompson, G. and Rona, P. (1991) Comparative mineralogy  
454 and geochemistry of gold-bearing sulfide deposits on the mid-ocean ridges. *Marine Geology*,  
455 101, 217-248.
- 456 Hofmann, A., Bekker, A., Rouxsel, O., Rumble, D., and Master, S. (2009) Multiple sulfur and iron  
457 isotope composition of detrital pyrite in Archean sedimentary rocks: A new tool for provenance  
458 analysis. *Earth Planetary Science Letters*, 286, 436-445.
- 459 Hower, J.C., Campbell, J.L., Teesdale, W.J., Nejedny, Z., and Robertson, J.D. (2008) Scanning  
460 probe microprobe analysis of mercury and other trace elements in Fe-sulfides from a Kentucky  
461 coal. *International Journal of Coal Geology*, 75, 88-92.
- 462 Huston, D.L., Sie, S.H., Suter, G.F., Cooke, D.R., and Both, R.A. (1995) Trace elements in sulphide  
463 minerals from eastern Australian volcanic-hosted massive sulphide deposits: Part I. Proton  
464 microprobe analyses of pyrite, chalcopyrite, and sphalerite, and Part II. Selenium levels in pyrite:  
465 Comparison with <sup>34</sup>S values and implications for the source of sulphur in volcanogenic  
466 hydrothermal systems. *Economic Geology*, 90, 1167-1196.
- 467 Ikramuddin, M., Besse, L., and Nordstrom, P.M. (1986) Thallium in the Carlin-type gold deposit.  
468 *Applied Geochemistry*, 1, 493-502.

- 469 Ingham, E.S., Cook, N.J., Cliff, J., Ciobanu, C.L., and Huddleston, A. (2014) A combined chemical  
470 isotopic and microstructural study of pyrite from roll-front uranium deposits, Lake Eyre Basin,  
471 South Australia. *Geochimica et Cosmochimica Acta*, 125, 440-465.
- 472 Jamil, N.Y., and Shaw, D. (1994) The diffusion of Mn in CdSe. *Semicond. Sci. Technol.*, 10, 952-  
473 958.
- 474 John Peter, A.L., and Viraraghavan, T. (2005) Thallium: a review of public health and  
475 environmental concerns. *Environment International*, 31, 493-501.
- 476 Kazantzis, G. (2000) Thallium in the environment and health effects. *Environmental Geochemistry*  
477 *and Health*, 22, 275-280.
- 478 Keith, M., Häckel, F., Haase, K.M., Schwartz-Schampera, U., and Klemd, R. (2016) Trace element  
479 systematics of pyrite from submarine hydrothermal vents. *Ore Geology Reviews*, 72, 728-745.
- 480 Kolker, A (2012) Minor element distribution in iron disulfides in coal: A geochemical review.  
481 *International Journal of Coal Geology*, 74, 32-43.
- 482 Kouzmanov, K., Pettke, T., and Heinrich, C.A. (2010) Direct analysis of ore-precipitating fluids:  
483 Combined IR microscopy and LA-ICP-MS study of fluid inclusions in opaque ore minerals.  
484 *Economic Geology*, 105, 351-373.
- 485 Kyle, J.H., Breuer, P.L., Bunney, K.G., Pleysier, R., and May, P.M. (2011) Review of trace toxic  
486 elements (Pb, Cd, Hg, As, Sb, Bi, Se, Te) and their deportment in gold processing. Part 1:  
487 Mineralogy, aqueous chemistry and toxicity. *Hydrometallurgy*, 107, 91-100.
- 488 Large, R.R., Maslennikov, V.V., Robert, F., Danyushevsky, L., and Chang, Z. (2007) Multistage  
489 Sedimentary and metamorphic origin of pyrite and gold in the giant Sukhoi Log deposit, Lena  
490 gold province, Russia. *Economic Geology*, 102, 1233-1267.
- 491 Large, R.R., Danyushevsky, L., Hollit, C., Maslennikov, V.V., Meffre, S., Gilbert, S., Bull, S., Scott,  
492 R., Emsbo, P., Thomas, H., Singh, B., and Foster, J. (2009) Gold and trace elements zonation in  
493 pyrite using Laser Imaging Technique: Implications for the timing of gold in orogenic and  
494 Carlin-Style sediment-hosted deposits. *Economic Geology*, 104, 635-668.

- 495 Large, R.R., Halpin, J.A., Danyushevsky, L.V., Maslennikov, V.V., Bull, S.W., Long, J.A., Gregory,  
496 D.D., Lounejeva, E., Lyons, T.W., Sack, P.J., McGoldrick, P.J., and Calver, C.R. (2014) Trace  
497 element content of sedimentary pyrite as a new proxy for deep-time ocean-atmosphere evolution.  
498 Earth Planetary Science Letters, 389, 209-220.
- 499 Lefticariu, L., Blum, J.D., and Gleason, J.D. (2011) Mercury isotopic evidence for multiple mercury  
500 sources in coal from the Illinois Basin. Environmental Science & Technology, 45, 1724-1729.
- 501 Lehner, S.W., Savage, K., and Ayers, J.C. (2006) Vapour growth and characterization of pyrite  
502 (FeS<sub>2</sub>) doped with Ni, Co, and As: Variations in semiconducting properties. Journal of Crystal  
503 Growth, 286, 306-317.
- 504 Lehner, S.W., Newman, N., van Schilfgaarde, M., Bandyopadhyay, S., Savage, K., and Buseck, P.  
505 (2012) Defect energy levels and electronic behaviour of Ni-, Co-, and As-doped synthetic pyrite  
506 (FeS<sub>2</sub>). Journal of Applied Physics, 111, 083717.
- 507 Li, N., Deng, J., Yang, L.-Q., Goldfarb, R.J., Zhang, C., Marsh, E., Lei, S.-B., Koenig, A., and  
508 Lowers, H. (2014). Paragenesis and geochemistry of ore minerals in the epizonal gold deposits  
509 of the Yangshan gold belt, West Qinling, China. Mineralium Deposita, 49, 427-449.
- 510 Lockington, J.A., Cook, N.J., and Ciobanu, C.L. (2014) Trace and minor elements in sphalerite  
511 from metamorphosed sulphide deposits. Mineralogy and Petrology, 108, 873-890.
- 512 Marin-Carbonne, J., Rollion-Bard, C., Bekker, A., Rouxel, O., Agangi, A., Cavalazzi B.,  
513 Wohlgemuth-Ueberwasser, C.C., Hofmann, A., and McKeegan, K.D. (2014) Coupled Fe and S  
514 isotope variations in pyrite nodules from Archean shale. Earth Planetary Science Letters, 392,  
515 67-79.
- 516 Okamoto, H., and Massalski, T.B. (1987) Phase diagrams of binary gold alloys. ISBN: 0-87170-  
517 249-5; 0-87170-249-5
- 518 Okrusch, M., Lorenz, J.A., and Weyer, S. (2007) The genesis of sulphide assemblages in the former  
519 Wilhelmine mine, Spassart, Bavaria, Germany. Canadian Mineralogist, 45, 723-750.
- 520 O'Shaughnessy, T.A., Barber, H.D., Thompson, D.A., and Heasell, E.L. (1974) The solid solubility

- 521 of gold in doped silicon by oxide encapsulation. *Journal of Electrochemical Society*, 121, 1350-  
522 1354.
- 523 Pačevski, A., Moritz, R., Kouzmanov, K., Marquart, K., Živković, P., and Cvetković, L. (2012)  
524 Texture and composition of Pb-bearing pyrite from the Čoka Marin polymetallic deposit, Serbia,  
525 controlled by nanoscale inclusions. *The Canadian Mineralogist*, 50, 1-20.
- 526 Palenik, C.S., Ustunomiya, S., Reich, M., Kesler, S.E., Wang, L., and Ewing, R.C. (2004)  
527 “Invisible” gold revealed: Direct imaging of gold nanoparticles in a Carlin-type deposit.  
528 *American Mineralogist*, 89, 1359-1366.
- 529 Palenova, E.E., Belogub, E.F., Plotinskaya, O. Yu., Novoselov, K.A., Maslennikov, V.V., Kotlyarov,  
530 V. A., Blinov, I.A., Kuzmenko, A.A., and Griboyedova, I.G. (2015) Chemical evolution of pyrite  
531 at the Kopylovsky and Kavkaz Black shale-hosted gold deposits, Bodaybo District, Russia:  
532 Evidence from EMPA and LA-ICP-MS data. *Geology of Ore Deposits*, 57, 64-84.
- 533 Parkman, R.H., Charnock, J.M., Bryan, N.D., Livens, F.R., and Vaughan, D.J. (1999) Reactions of  
534 copper and cadmium ions in aqueous solution with goethite, lepidocrocite, mackinawite, and  
535 pyrite. *American Mineralogist*, 84, 407-419.
- 536 Pass, H.E. (2010) Breccia-hosted chemical and mineralogical zonation patterns of the northeast zone,  
537 Mt. Polley Cu-Ag-Au alkali porphyry deposit, British Columbia, Canada. Ph.D. thesis.  
538 University of Tasmania.
- 539 Pearce, C.I., Patrick, R.A.D., and Vaughan, D.J. (2006) Electrical and magnetic properties of  
540 sulphides. *Review in Mineralogy and Geochemistry*, 61, 127-180.
- 541 Pirrone, N., Cinnirella, S., Feng, X., Finkelman, R.B., Friedli, H.R., Leaner, J., Mason, R.,  
542 Mukherjee, A.B., Stracher, G.B., Streets, D.G., and Telner, K. (2010) Global mercury emissions  
543 to the atmosphere from anthropogenic and natural resources. *Atmospheric Chemistry and*  
544 *Physics*, 10, 5951-5964.
- 545 Plant, J.A.; Bone, J.; Voulvoulis, N.; Kinniburgh, D.G.; Smedley, P.L.; Fordyce, F.M.; Klinck, B..  
546 (2014) Arsenic and selenium. In: Holland, H.D.; Turekain, K.K., (eds.) *Environmental*

- 547 geochemistry. Oxford, UK, Elsevier, 13-57. (Treatise on Geochemistry, 11).
- 548 Revan, M.K., Genc, Y., Maslennikov, V.V. Maslennikova, S.P., Large, R.R., and Danyushevsky,  
549 L.V. (2014) Mineralogy and trace-element geochemistry of sulphide minerals in hydrothermal  
550 chimneys from the Upper-Cretaceous BMS deposits of the eastern Pontide orogenic belt (NE  
551 Turkey). *Ore Geology Reviews*, 63, 129-149.
- 552 Reich, M., Kesler, S.E., Utsunomiya, S., Palenik, C.S., Chryssoulis, S.L., and Ewing, R.C. (2005)  
553 Solubility of gold in arsenian pyrite. *Geochimica et Cosmochimica Acta*, 69, 2781-2796.
- 554 Reich, M., Utsunomiya, S., Kesler, S.E., Wang, L.M., Ewing, R.C., and Becker, U. (2006) Thermal  
555 behaviour of metal nanoparticles in geologic materials. *Geology*, 34, 1033-1036.
- 556 Reich, M., Palacios, C., Chryssoulis, S., Weldt, M., Alvear, M., and Deditius, A. (2010) “Invisible”  
557 silver and gold in supergene chalcocite. *Geochimica et Cosmochimica Acta*, 74, 6157-6173.
- 558 Reich, M. Deditius, A. P., Chryssoulis, S., Li, J.W., Ma, C.Q., Parada, M.A., Barra, F., and  
559 Mittermayr, F. (2013) Pyrite as a record of hydrothermal fluid evolution in a porphyry copper  
560 system: A SIMS/EMPA trace element study. *Geochimica et Cosmochimica Acta*, 104, 42–62.
- 561 Rickard, D., and Luther, III G.W. (2007) Chemistry of iron sulphides. *Chemistry Reviews*, 107,  
562 514-562.
- 563 Schackelton, J.M., Spry, P.G., and Bateman, R. (2003) Telluride mineralogy of the Golden Mile  
564 deposit Kalgoorlie, Western Australia. *The Canadian Mineralogist*, 41, 1503-1524.
- 565 Scher, S., Williams-Jones, A.E., and Williams-Jones, G. (2013) Fumarolic activity, acid-sulfate  
566 alteration, and high-sulfidation epithermal precious metal mineralization in the crater of Kawah  
567 Ijen volcano, Java, Indonesia. *Economic Geology*, 108, 1099-1118.
- 568 Schopf, C., Martin, A., Schmidt, M., and Lacopino, D. (2015) Investigation of Au-Hg amalgam  
569 formation on substrate-immobilized individual Au nanorods. *Journal of Materials Chemistry C*,  
570 3, 8865-8872.
- 571 Scott, R.J., Meffre, S., Woodhead, J., Gilbert, S.E., Berry, R.F., and Emsbo, P. (2009) Development  
572 of framboidal pyrite during diagenesis, low-grade regional metamorphism, and hydrothermal



- 573 alteration. *Economic Geology*, 104, 1143-1168.
- 574 Shannon, R.D. (1976) Revised effective ionic radii and systematic studies of interatomic distances  
575 in halides and chalcogenides. *Acta Crystallographica B*, A32, 751-767.
- 576 Simon, G., Huang, H., Penner-Hahn, J.E., Kesler, S.E., and Kao, L.-S. (1999) Oxidation state of  
577 gold and arsenic in gold-bearing arsenian pyrite. *American Mineralogist*, 84, 1071-1079.
- 578 Steadman, J.A., Large, R.R., Meffre, S., Olin, P.H., Danyushevsky, L.V., Gregory, D.D., Belousov,  
579 I., Louneyeva, E., Ireland, T.R., and Holden, P. (2015) Synsedimentary to early diagenetic gold  
580 in black shale-hosted pyrite nodules at the Golden Mile deposit, Kalgoorlie, Western Australia.  
581 *Economic Geology*, 110, 1157-1191.
- 582 Su, W., Zhang, H., Hu, R., Ge, X., Xia, B., Chen, Y., and Zhu, C. (2012) Mineralogy and  
583 geochemistry of gold-bearing arsenian pyrite from Shuiyidong Carlin-type gold deposit,  
584 Guizhou, China: implications for gold depositional processes. *Mineralium Deposita*, 47, 653-  
585 662.
- 586 Sunagawa, I., and Takahashi, K., (1955) Preliminary report on the relation between o(111) face of  
587 pyrite crystals and its minor contents of arsenic. *Geological Society of Japan Bulletin*, 6, 1-10.
- 588 Sung, Y.-H., Brugger, J., Ciobanu, C.L., Pring, A., Skinner, W., and Nugus, M. (2009) Invisible gold  
589 in pyrite and arsenopyrite from multistage Archean gold deposits: Sunrise Dam Eastern  
590 Goldfields Province. *Mineralium Deposita*, 44, 765-791.
- 591 Thomas, H.V., Large, R.R., Bull, S.W., Masslennikov, V., Berry, R.F., Fraser, R., Froud, S. and  
592 Moye, R. (2011) Pyrite and pyrrhotite textures and composition in sediments, laminated quartz  
593 veins, and reefs at Bendigo gold mine, Australia: Insights for ore genesis. *Economic Geology*,  
594 106, 1-31.
- 595 Tomkins, A.G., Pattison, D.R.M., and Frost, B.R. (2007) On the initiation of the metamorphic  
596 sulfide anatexis. *Journal of Petrology*, 48, 511-535.
- 597 Wang, C., Chen, Y., Pan, J., Zhang, P., Qi, J., Liu, J., Li, X., and Wang, J. (2010) Speciation analysis  
598 of metals (Tl, Cd and Pb) in Tl-containing pyrite and its cinder from Yunfu Mine, China, by La-

- 599 ICP-MS with sequential extraction. *Chinese Journal of Geochemistry*, 29, 113-119.
- 600 Wood, B.L., and Large, R.R. (2007) Syngenetic gold in western Victoria: occurrence, age and  
601 dimensions. *Australian Journal of Earth Science*, 54, 711-732.
- 602 Yang, J., and Ying, J.Y. (2010) Diffusion of gold from the inner core to the surface of Ag<sub>2</sub>S  
603 nanocrystals. *Journal of American Chemical Society*, 132, 2114-2115.
- 604 Yudovskaya, M.A., Distler, V.V., Chaplygin, I.V., Mokhov, A.V., Trubkin, N.V., and Gorbacheva,  
605 S.A. (2006) Gaseous transport and deposition of gold in magmatic fluid: evidence from the  
606 active Kydryavy volcano, Kurile Islands. *Mineralium Deposita*, 40, 828-848.
- 607 Zelenski, M., and Bortnikova, S. (2005) Sublimate speciation at Mutnovsky volcano, Kamchatka.  
608 *European Journal of Mineralogy*, 17, 107-118.
- 609 Zhang, J.Y., Ren, D., Zheng, C.G., Zeng, R.S., Chou, C.L., and Liu, J. (2002) Trace element  
610 abundances in major minerals of Late Permian coals from southwestern Guizhou province,  
611 China. *International Journal of Coal Geology*, 53, 55-64.
- 612 Zhou, T.F., Fan, Y., Yuan, F., Wu, M.A., Hou, M.J., Voicu, G., Hu, Q.H., Zhang, Q.M., and Yue,  
613 S.C. (2005) A preliminary geological and geochemical study of the Xiangquan thallium deposit,  
614 eastern China: the world's first thallium-only mine. *Mineralogy and Petrology*, 85, 243-251.
- 615 Zhou, T., Fan, Y., Yuan, F., Cooke, D., Zhang, X., and Li, L. (2008) A preliminary investigation and  
616 evaluation of the thallium environmental impacts of the unmined Xiangquan thallium-only  
617 deposit in Hexian, China. *Environmental Geology*, 54, 131-145.

618

### 619 **Figure captions**

620 **Figure 1.** Concentrations of Hg, Tl, and Cd as a function of As concentration in pyrite (in ppm; log-  
621 log scale). Grey solid line depicts the solubility limit of Au in pyrite as a function of As content after  
622 Reich et al. (2005). Distribution of the analyses in metal-As log-log space as a function of the type  
623 of ore deposit. (A) Solubility limit of Hg in arsenian pyrite compared to the solubility of Au in  
624 arsenian pyrite. (B) Solubility limit of Tl in arsenian pyrite compared to the solubility of Au in

625 arsenian pyrite. (C) Concentration of Cd vs. As in arsenian pyrite compared to the solubility of Au  
626 in arsenian pyrite. Note the thick, black, dashed line outlining the data points that represent Cd-rich  
627 sphalerite inclusions in pyrite from VMS deposits and hydrothermal vents. The summary of  
628 literature data is provided in [Table 1](#).

629 **Figure 2.** Solubility of metals (Au, Hg, Tl) in arsenian pyrite in As-metal-T (log-log-°C) space.

630 Note the shift of the solubility limit along the solubility place as a function of changing temperature.

Figure 1

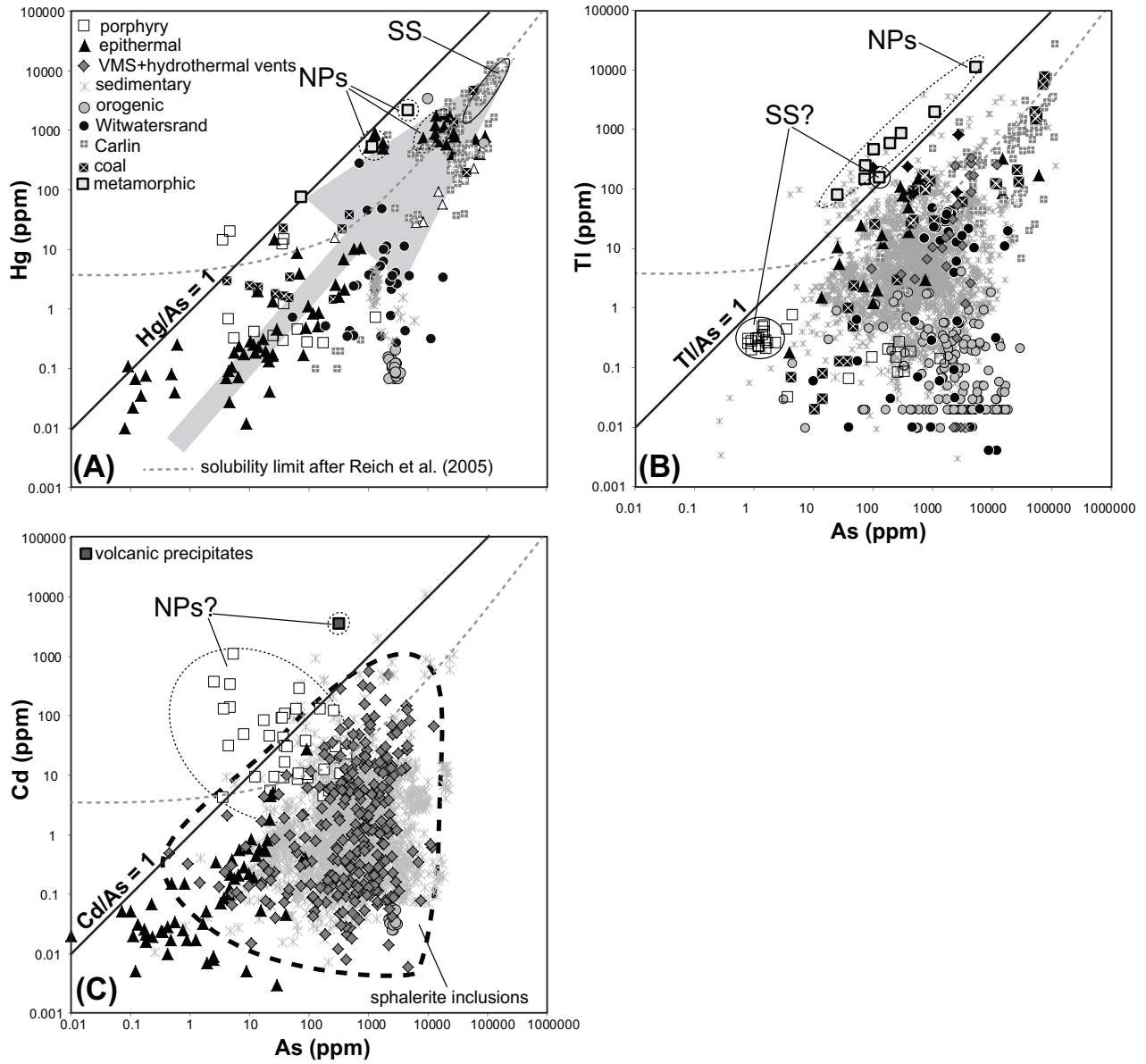


Figure 2

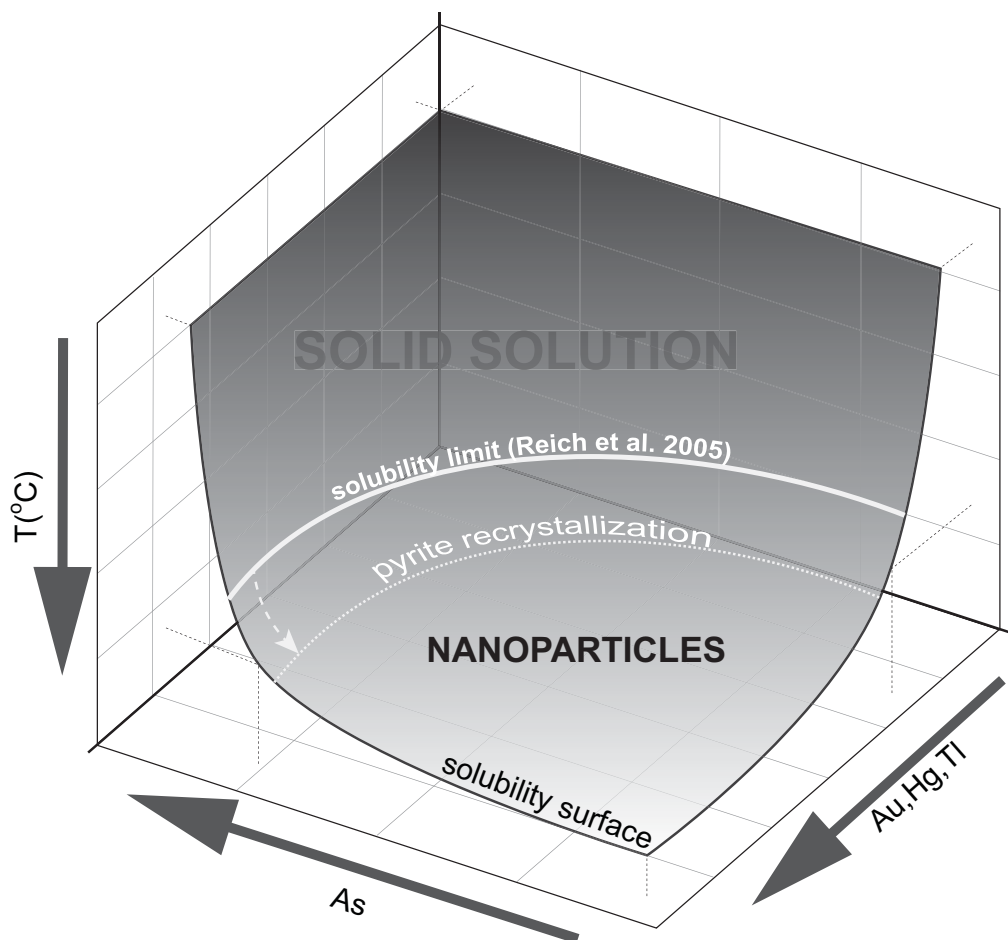


Table 1. List of the discussed deposits.

REFERENCE	TYPE OF ORE DEPOSIT	ELEMENTS			LOCALITY, MINERAL ASSEMBLAGE (MA)*, INCLUSIONS (INCL)	ANALYTICAL METHODS
		Hg	Tl	Cd		
Scott et al. (2009)	Sedimentary	--	X	--	Fosterville (Victoria, Australia); MA: py, gn, INCL: N/D	LA-ICP-MS
Hoffman et al. (2009)			X		Belingwe Greenstone Belt (Zimbabwe); South Africa; MA* and INCL** - N/D ***	HR-ICP-MS
Berner et al. (2013)		--	X	X	Posidonia Shale (Germany); MA: N/D; INCL: - sph	IC P-MS
Ingham et al. (2014)		--	X	--	roll-front Beverly North uranium deposits (South Australia); MA: py, sph, Se; INCL: Se,	LA-ICP-MS
Large et al. (2014)		--	X	X	Black shale (numerous localities); MA and INCL: N/D	LA-ICP-MS
Marin-Carbonne et al. (2014)		X	X	--	Carbonaceous shales, Bubi Greenstone Belt (Zimbabwe); MA: N/D; INCL: cpy	EMPA, LA-ICP-MS
Palenova et al.(2015)		X	X	X	Kopylovsky and Kavkaz (black shale) (Russia); MA: py, Au, po, cpy, gn, sph,mar, pn, vio, mil, gers, ulm, cob, asp, mo; INCL: Au, cpy, po, gn,	EMPA, LA-ICP-MS
Staedman et al. (2015)		--	X	--	Golden Mile (black shales) (Australia); MA: py, cpy, cas, sph, po, asp, ull; INCL: sph, cpy, ten, Au, Au-tellurides	LA-ICP-MS
Zhang et al. (2002)	Coal	X	X	--	SW Guizhou province (China); MA and INCL: N/D	ICP-MS
Ding et al. (2001)		X	--	--	SW Guizhou Province (China); MA: py, asp, rlg; INCL: N/D	EMPA, INAA
Zhou et al. (2008)		--	X	--	Xiangquan (Hexian, China); MA: N/D; INCL: Tl-bearing grains	ICP-MS
Hower et al. (2009)		X	X	--	Manchester coal bed, Clay County, (Kentucky, USA); MA: py, mar, claus; INCL:	Micro-PIXE
Cline (2001)	Carlin-type	X	X	--	Getchell, Nevada (USA); MA: py, cpy, asp, gn, sph, mar, stb, rlg; INCL: N/D	EMPA, SIMS
Emsbo et al. (2003)		X	X	--	Meikle, (USA); MA: Au, py, (As,Au)-py, mc, asp, tetr, sph, stb, HgTe, AgTe; INCL: N/D	EMPA, SIMS
Reich et al. (2005)		X	--	--	Deep Star, (Nevada, USA); MA and INCL: N/D	EMPA, SIMS
Su et al. (2012)		X	--	--	Shuiyindong, (Guizhou, China); MA: py, asp, mar, orp, rlg, stb; INCL: asp, Au,	EMPA
Barker et al. (2009)		X	X	--	West Banshee, Turquoise Ridge, (Nevada, USA); MA: py, asp, orp, rea; INCL: N/D	EMPA, SIMS
Deditius et al. (2011)		X	--	--	Deep Star (Nevada, USA); MA: N/D; INCL: (Ag,Pb)-sulfides, Au, Ag Screamer (Nevada, USA); MA: N/D; INCL: cin Lone Tree (Nevada, USA); MA: N/D; INCL: (Au,Ag,As,Ni)-sulphide, (Fe,As,Ag,Ni)-sulphide, (Fe,As,Sb,Pb,Ni,Au)-sulphide	EMPA, SIMS
Large et al. (2009)		--	X	--	Rodeo, Meikle, Gold Quarry (Nevada, USA); MA: py, marc; INCL - N/D	LA-ICP-MS
Scott et al. (2009)		--	X	--	Goldstrike, Gold Quarry, (Nevada, USA); MA: py, mar; INCL: N/D	LA-ICP-MS
Gryffin et al. (1991)	Epithermal	X	X	--	North Arm (Queensland, Australia); MA: py, mar, sph, cpy, Ag, Au, naum, frei, asp; INCL: mar, Au, Ag, cpy, sph, gn, po, mo.	PIXE
Cepedal et al. (2008)		X	--	--	El Valle (Spain); MA: py, po, marc, asp, tetr, and, gud, cpy, cov, gn, sph, gr; INCL: asp,	EMPA
Reich et al. (2005)		X	--	--	Porgera (Papua New Guinea); ; MA and INCL: N/D	EMPA, SIMS
Okrush et al. (2007)		X	--	--	Wilhelmine mine, (Bavaria, Germany); MA: py, enarg, ten, cpy, bor, dig, dju; INCL: N/D	EMPA
Deditius et al. (2011)		X	--	--	Pueblo Viejo (Dominican Republic); MA: py, enar; INCL: (Pb,Bi,Sb,Ag,Te)-sulphide; Au, Ag, Au-telluride; Ag-Sb. Porgera (Papua New Guinea); MA: N/D; INCL: gn, (Pb,Ag,Sb)-sulphides	EMPA, SIMS
Scher et al. (2013)		X	X	X	Kawah Ijen volcano, Java (Indonesia); MA: N/D; INCL: mo, bis, gn, sph.	LA-ICP-MS
Franchini et al. (2015)		X	--	X	Agua Rica Cu (Mo-Au) (Argentina) (high-sulfidation epithermal part); MA: py, mo, mar, sph, en, kur, cv; INCL: cpy, bn, po,	LA-ICP-MS
Kozmanov et al. (2010)	Porphyry	--	X	--	High-sulphidation epithermal veins overprinting porphyry Cu, Rosia Poieni (Romania); MA-py,en, mo, col, Au-Ag-Bi tellurides, ten, cpy, bn, dig, cov, Te; INCL: cpy, en, bn, cov, Ag-Au tellurides or selenides.	EMPA, LA-ICP-MS
Pass et al. (2010)		X	X	X	Mt. Polley, (British Columbia, Canada); MA: py, cpy, bor; INCL: cpy, gn, sph, Au, telluride; Pt-Pd-bearing minerals	LA-ICP-MS
Large et al. (2007)	Orogenic gold	--	X	--	Sukhoi Log (Russia); MA: py, asp, po, Au, Au-tellurides; INCL: Au, asp, po, sph, cpy, gn	LA-ICP-MS

Large et al. (2009)					Bendigo (Australia); MA: N/D; INCL: cpy, gn Sukhoi Log (Russia); MA: N/D; INCL: sph, cpy, po, gn, Au Spanish Mt. (Canada); MA: N/D; INCL: cpy, sph, gn	LA-ICP-MS
Wood and Large (2007)		--	X	--	Western Victoria (Australia) – localities in Table 2 therein; MA and INCL: N/D	LA-ICP-MS
Large et al. (2009)		--	X	--	Spanish Mt., (Canada); MA-N/D; INCL: Au, sph, gn, cpy; Sukhoi Log, (Russia); MA: N/D; INCL: Au, sph, cpy, gn, po; Bendigo, (Australia); MA-N/D; INCL: cpy, gn, Pb-Bi-Au tellurides	LA-ICP-MS
Shackleton et al. (2003)		X	--	--	Golden Mile (Australia); MA: py, asp, po, sph, cpy, cv, Au, Te, precious metals tellurides; INCL: Au, clv, syl, kren, ptz.	EMPA
Thomas et al. (2011)		--	X	--	Bendigo, (Australia); MA: py, Au, sph, asp, po, gn; INCL: gn	LA-ICP-MS
Deol et al. (2012)		--	X	--	Bhukja-Jaggpura (India); MA: py, asp, po, cpy; INCL: Au,	EMPA, LA-ICP-MS
Cabral et al. (2013)		X	--	X	Antônio Pareira (Brazil); MA: py, asp, po; INCL: N/D	LA-ICP-MS
Li et al. (2014)		--	X	--	Getiaowan-Anba gold deposits, Yangshan gold belt (China); MA: py, MA and INCL: asp, Au, stb, sph, gn, cpy, ten, jam, boul, fam	EMPA, LA-ICP-MS
Duchesne et al. (1983)	Pb-Zn	--	X	--	Pb-Zn deposits (Belgium); MA: py, mar; INCL: hut	SIMS
Revan et al. (2014)	VMS	--	X	X	Pontide orogenic belt (Turkey); MA: py, cpy, sph, gn, bn, Au, Ag, ma, cc, cv, en, Bi, tet, dgn, gersd, INCL: (Au,Ag)-tellurides	LA-ICP-MS
Genna and Gaboury (2015)		--	X	X	Bracemac-McLeod (Canada); MA: py, cpy, gn, sph, INCL: cpy, gn, sph, Ag-Au-Te,	LA-ICP-MS
Agangi et al. (2013)	Witwatersrand	X	--	--	INCL: cpy, gn, Au, sph, po, Au-Ag-Hg alloy,	EMPA, LA-ICP-MS
Yudovskaya et al. (2006)	Volcanic precipitates	--	--	X	Kudryavy volcano (Kurile Islands; Russia); MA: py, gn, sph, cov, cpy, cc, Pb <sub>3</sub> Bi <sub>6</sub> S <sub>13</sub> , TlCl; INCL: N/D	INAA
Zelenski and Bortnikova (2005)		X	X	X	Mutnovsky volcano, Kamchatka (Russia); MA: py, po, gn, gr, Cd-sulfosalts, Tl; INCL: N/D	EMPA
Biagioni et al. (2013)	Metamorphic	X	X	--	Alpi Apuane (Italy); MA: py, cinnabar, realgar, sph, stb, twinnite, polhemusite, Tl-Hg-As-Sb-Ag-Pb sulfosalts;	EMPA, ICP-MS

\*MA - Mineral assemblage – the information is limited to minerals that might contaminate pyrite with Hg, Tl, and Cd. \*\*INCL – inclusions in pyrite; \*\*\*N/D – no data;

Mineral abbreviations: and – andorite, ani – anilite, asp – arsenopyrite, bis – bismuthinite, bn – bornite, boul – boulangerite, cas – cassiterite, cc – chalcocite, cal – calaverite, cob – cobaltite, clau – clausthalite, cv – covellite, col – colusite, cpy – chalcopyrite, dig – digenite, dju – djurleite, en – enargite, fam – faminite, frei – freibergite, gersd – gersdorffite, gn – galena, gr – greenockite, gud – gudmundite, hut – hutchinsonite, ida – idaite, jam – jamesonite, kren – krennerite, kur – kuramite, mar – marcasite, mil – millerite, mo – molybdenite, naum – naumannite, orp – orpiment, pn – pentlandite, po – pyrrotite, py – pyrite, ptz – petzite, rlg – realgar, sph – sphalerite, spi – spinkopite, stb – stibnite, ten – tennantite, tet – tetrahedrite, ull - , ulm - , vio – violarite, yar – yarrowite.